

Phase Distribution and Carrier Dynamics in Multiple-Ring Aromatic Spacer-Based Two-Dimensional Ruddlesden–Popper Perovskite Solar Cells

Zhiyuan Xu, Di Lu, Feng Liu, Hongtao Lai, Xiangjian Wan, Xiaodan Zhang, Yongsheng Liu,* and Yongsheng Chen



Cite This: *ACS Nano* 2020, 14, 4871–4881



Read Online

ACCESS |



Metrics & More



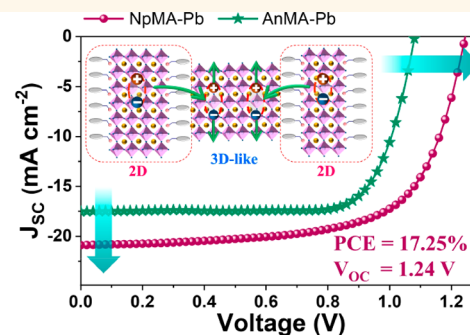
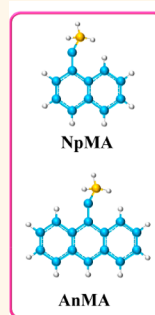
Article Recommendations



Supporting Information

ABSTRACT: Two-dimensional (2D) perovskites with natural multi-quantum-well structure have been reported to offer better stability compared to 3D perovskites. However, the understanding of the exciton separation and transport mechanism in 2D perovskites and developing more efficient organic spacers remain considerable challenges, as the 2D perovskites exhibit large exciton binding energy due to quantum confinement. Here, a class of multiple-ring aromatic ammoniums, 1-naphthalenemethylammonium (NpMA) and 9-anthracenemethylammonium (AnMA), was developed as spacers for 2D Ruddlesden–Popper (RP) perovskite solar cells (PSCs). In addition to significantly enhanced stability, the device based on $(\text{NpMA})_2(\text{MA})_{n-1}\text{Pb}_n\text{I}_{3n+1}$ (average $n = 4$) exhibits a champion efficiency of 17.25% and a high open-circuit voltage of 1.24 V. The outstanding photovoltaic performance could be ascribed to the ultrafast exciton migration (within 7 ps) from 2D phases to 3D-like phases, which were confirmed by charge carrier dynamics results, leading to efficient exciton separation, charge transportation, and collection. This work facilitates understanding the working mechanism of 2D PSCs in-depth and offers an efficient way to further boost their efficiency and stability by developing multiple-ring aromatic spacers.

KEYWORDS: perovskite solar cell, organic spacer, two-dimensional, phase distribution, charge transport



Metal halide perovskite solar cells (PSCs) have gained enormous attention due to their low fabrication cost and high photovoltaic performance, which bring a true revolution in photovoltaic technology.^{1–3} The power conversion efficiencies (PCEs) have been improved from 3.8% in 2009 to a certified 25.2% recently due to the good properties of perovskite materials, such as high absorption coefficient, long charge-carrier diffusion length, and excellent defect tolerance.^{4–8} As the efficiency of PSCs is close to the monocrystalline silicon solar cells, attention is increasingly focused on the stability issues of the perovskite materials and devices.^{9,10} Although various efforts have been conducted to improve the device stability, such as interface engineering, precursor solution engineering, and device encapsulation, it is still a great challenge to realize long-term stability.^{11–13}

Two-dimensional (2D) Ruddlesden–Popper (RP) perovskites with large-size organic spacers have attracted increasing attention owing to their superior ambient stability over their

3D counterparts.¹⁴ The improved stability is ascribed to the hydrophobicity of organic spacers in the 2D perovskite lattice as well as the suppressed ion migration.^{15,16} The general chemical formula of 2D RP perovskites can be described as $\text{A}_2\text{B}_{n-1}\text{M}_n\text{X}_{3n+1}$.¹⁷ Here, A represents a monovalent organic spacer cation; B represents a monovalent cation; M represents a divalent metal cation; X is a halide anion; and n refers to the number of MX_6^{4-} octahedral layers.¹⁷ To date, most organic spacers used in 2D RP perovskites are insulating aliphatic or single-ring aromatic cations, such as n -butylammonium (BA), phenethylammonium (PEA), and 4-fluoro-

Received: January 31, 2020

Accepted: April 2, 2020

Published: April 3, 2020



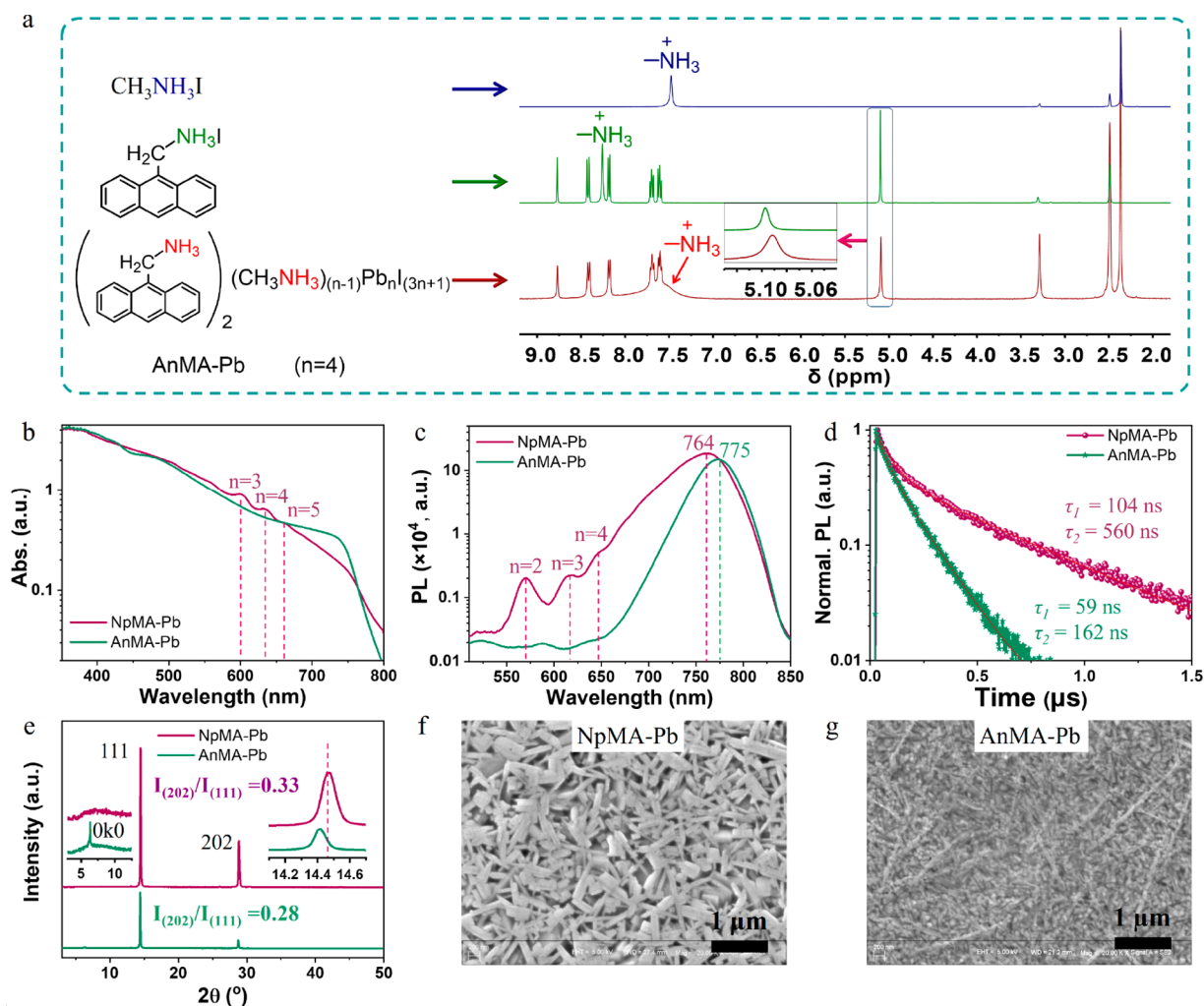


Figure 1. (a) Chemical structure and corresponding ^1H NMR spectra showing changes in the resonance signals arising from the H protons of MAI, AnMAI, and AnMA-Pb. (b) UV-vis absorption spectra of the NpMA-Pb and AnMA-Pb films. (c, d) PL and TRPL spectra of the NpMA-Pb and AnMA-Pb films excited from back sides. (e) XRD patterns of the NpMA-Pb and AnMA-Pb films. (f, g) SEM images of the NpMA-Pb and AnMA-Pb films.

phenethylammonium, which exhibit weak light-absorbing properties.^{18–27} The multiple-ring aromatic ammoniums with extensive π -electron delocalization in the conjugated backbone are expected to enhance charge transport and absorb more solar light than that of an inorganic framework, thus increasing the current and efficiency of the photovoltaic devices. In 1999, Mitzi and co-workers reported a quaterthiophene-based 2D RP perovskite, and the absorption spectra of thermally ablated films exhibit an exciton peak arising from the corner-sharing $[\text{PbI}_6]^{4-}$ sheets, along with absorption from the quaterthiophene moiety.^{28,29} Acene-based 2D RP perovskites were also studied due to the tunable number of fused benzene rings in the acene group (e.g., phenyl-, naphthyl-, and anthryl-), which could impact the size and highest occupied molecular orbital–lowest unoccupied molecular orbital (HOMO–LUMO) separation of the aromatic spacer.^{30,31} Note that the naphthyl-based 2D RP perovskites have been used in light-emitting diodes and show a very high external quantum efficiency.^{32,33} However, the multiple-ring aromatic spacer-based 2D PSCs were rarely studied, possible because of the poor solubility of multiple-ring aromatic ligands or lack of suitable film-processing methods to obtain high-quality films.^{29,34} In addition, compared to 3D perovskites, 2D

perovskites exhibit much larger exciton binding energy due to quantum confinement, and it can be as high as 300 meV for low n -value layered perovskites, which makes it difficult for excitons to dissociate into free carriers *via* thermal energy activation at room temperature.³⁵ Although the efficiency of 2D RP perovskite solar cells increased quickly, the mechanism of the exciton migration and separation in 2D perovskite is still a matter of considerable debate.^{35–38} Therefore, the development of more efficient organic spacers and understanding the charge separation and transport mechanism in depth become particularly important to further boosting the photovoltaic performance of 2D PSCs for future commercialization.

In this work, we developed two multiple-ring spacer cations, 1-naphthalenemethylammonium (NpMA) and 9-anthracenemethylammonium (AnMA), for 2D RP perovskites and demonstrated highly efficient solar cells with a nominal $n = 4$ average composition. We found that the different layered phases and 3D-like phases coexist in the perovskite film. By performing ^1H NMR spectroscopy, we confirmed the existence of strong hydrogen-bonding interactions between organic spacer cations (NpMA and AnMA) and inorganic layers. The phase distribution and crystal orientation in these 2D RP perovskites provide a deep understanding of the effect of

multiple-ring aromatic ammoniums (NpMA and AnMA) on properties of 2D perovskites. By using high-resolution transmission electron microscopy (HRTEM) and ultrafast transient absorption (TA) spectroscopy to probe the phase distribution and charge carrier dynamics, we found an ultrafast exciton migration process (within 7 ps) between small- n value 2D phases and large- n value 3D-like phases, resulting in efficient exciton separation, charge transport, and collection. The optimized devices showed a high open-circuit voltage (V_{OC}) of 1.24 V and a champion PCE up to 17.25% for NpMA-Pb-based devices. Moreover, owing to the superior hydrophobicity of multiple-ring aromatic spacers and the strong hydrogen-bonding interactions between organic spacer cations (NpMA and AnMA) and inorganic layers, the 2D RP PSCs show enhanced stability in comparison with that of 3D PSCs.

RESULTS AND DISCUSSION

Structure and Photophysical Properties. The 2D RP perovskite (NpMA)₂MA _{$n-1$} Pb _{$n-3n+1$} (NpMA-Pb, $n = 4$) and (AnMA)₂MA _{$n-1$} Pb _{$n-3n+1$} (AnMA-Pb, $n = 4$) thin films were prepared by a one-step spin-coating method. The detailed synthetic procedures and characterization data for NpMAI and AnMAI are given in the Supporting Information (Schemes S1 and S2). To probe the formation of 2D perovskites and the existence of hydrogen-bonding interactions between organic spacer cations (NpMA and AnMA) and inorganic layers, we performed ¹H NMR measurements. As shown in Figure 1a, the proton signal of the -NH₃⁺ groups appears at 7.47 and 8.26 ppm for MAI and AnMAI, respectively. An obvious chemical shift was observed for proton signals of the -NH₃⁺ after the formation of 2D RP perovskites, suggesting the N-H...I⁻ hydrogen-bonding interaction between -NH₃⁺ and iodide anions in the [PbI₆]⁴⁻ framework.³⁹ Similarly chemical shifts of the proton signals in the -NH₃⁺ groups were also observed in the ¹H NMR spectra of MAI, NpMAI, and NpMA-Pb (Figures S1 and S2). Due to the different chemical environment caused by electronic cloud distribution, the chemical shifts of the protons in -CH₂- show an upfield shift for AnMA-Pb in comparison with that of AnMAI. The strong hydrogen-bonding interactions were further verified using X-ray photoelectron spectroscopy (XPS) shown in Figures S3 and S4. Two main peaks at 138.4 and 143.3 eV were observed for the control 3D film, which were assigned to the Pb 4f_{7/2} and Pb 4f_{5/2}, respectively.²² The I 3d_{5/2} and I 3d_{3/2} peaks were located at 619.1 and 630.6 eV, respectively. There is an obvious shift of the feature peaks toward lower values in the XPS spectra for NpMA-Pb and AnMA-Pb films in comparison with that of the control film, suggesting that the chemical bonding length of Pb-I in PbI₆⁴⁻ has been changed due to the strong hydrogen-bonding interaction between NpMA (or AnMA) cations and [PbI₆]⁴⁻. Due to NpMA exhibiting a lower steric resistance compared to AnMA, -NH₃ in NpMA could be closer to [PbI₆]⁴⁻, leading to a stronger hydrogen-bonding interaction, which results in a larger binding energy shift of Pb (4f) and I (3d) for NpMA-Pb.

The absorption spectra of NpMA- and AnMA-based 2D perovskites are shown in Figure 1b. There are several obvious excitonic peaks for NpMA-Pb perovskite films, corresponding to a distribution of perovskite phases with $n = 3, 4, 5$, and ∞ . This observation indicates that there are multiple perovskite phases in the NpMA-Pb film. However, no obvious excitonic peaks were observed for the AnMA-Pb film, most likely

ascribed to the weak crystallinity of the film, which is consistent with the X-ray diffraction (XRD) and scanning electron microscopy (SEM) results discussed below. For the AnMA-Pb film, a broad absorption at long wavelengths could be assigned to large n phases owing to the weak crystal orientation caused by larger spacer cation size.⁴⁰ The lack of obvious exciton peaks in absorption spectra for the AnMA-Pb film was further confirmed by its photoluminescence (PL) spectra. These features indicate that quantum confinement is not dominating in the AnMA-Pb film, and charges can effectively transport across neighboring inorganic layers. Accordingly, the absorption peak of AnMA-Pb films is red-shifted compared to NpMA-Pb. Note that the absorption edge of 2D perovskite films showed a similar bandgap compared to 3D perovskite films (Figure S5a), indicating that both NpMA-Pb and AnMA-Pb films exist 3D-like phases.

To gain further insight into the phase distribution and charge dynamics of NpMA-Pb and AnMA-Pb films, steady-state PL and time-resolved PL (TRPL) spectroscopies were performed. As shown in Figure 1c, the NpMA-Pb film exhibits stronger PL intensity than that of the AnMA-Pb film, indicating reduced charge carrier nonradiative recombination resulting from high film quality and low defect density, which is consistent with the XRD and SEM data discussed below.²³ The major PL peaks are located at 764 and 775 nm for NpMA-Pb and AnMA-Pb, respectively, which are related to the 3D-like phases. These peaks are blue-shifted in comparison with that of a 3D perovskite film (Figure S6) due to the quantum confinement effect of 2D RP perovskites.³⁷ The obvious exciton peaks and blue-shifted major PL peak in the NpMA-Pb film compared to the AnMA-Pb film indicate the formation of more layered perovskite phases in NpMA-based 2D perovskite. The TRPL decay curves (Figure 1d) were fitted by a biexponential decay function of time t : $f(t) = A_1 \exp(-t/\tau_1) + A_2 \exp(-t/\tau_2) + B$, where τ_1 and τ_2 are the lifetimes for the fast and slow recombination, respectively, A_1 and A_2 are the relative decay amplitude, and B is a constant.⁴¹ The detailed parameters are summarized in Table S1. The carrier lifetimes of the NpMA-Pb film were calculated to be 104 and 560 ns for τ_1 and τ_2 , respectively. The AnMA-Pb film shows carrier lifetimes of 59 ns for τ_1 and 162 ns for τ_2 , which are shorter than that of the NpMA-Pb film. The significantly increased lifetime for the NpMA-Pb film could be attributed to its excellent crystallinity with nanorod morphology (Figure 1f), leading to suppressed nonradiative recombination, which was further confirmed by the calculated defect density in perovskite films as discussed below.

Crystal Orientation and Surface Morphology. The crystallographic orientation and crystallinity of 2D RP perovskite films were investigated by XRD. As shown in Figure 1e, the NpMA-Pb film exhibits stronger diffraction peaks than that of the AnMA-Pb film, suggesting enhanced crystallinity. Two distinct diffraction peaks were observed at around 14.4° and 28.7°, which can be assigned to the (111) and (202) lattice planes of 2D perovskites, respectively. The lack of (0k0) peaks below 10 degrees for the NpMA-Pb film indicates the 2D RP perovskite layers grow mainly along a vertical direction to the substrate, which facilitates efficient charge transport between the top and bottom electrodes.⁴⁰ Note that one distinct diffraction peak was observed at around 6.3° for the AnMA-Pb film (Figure S7a), which could be assigned to the diffraction peak of (0k0), suggesting the corner-sharing [PbI₆]⁴⁻ sheets grow along both parallel and

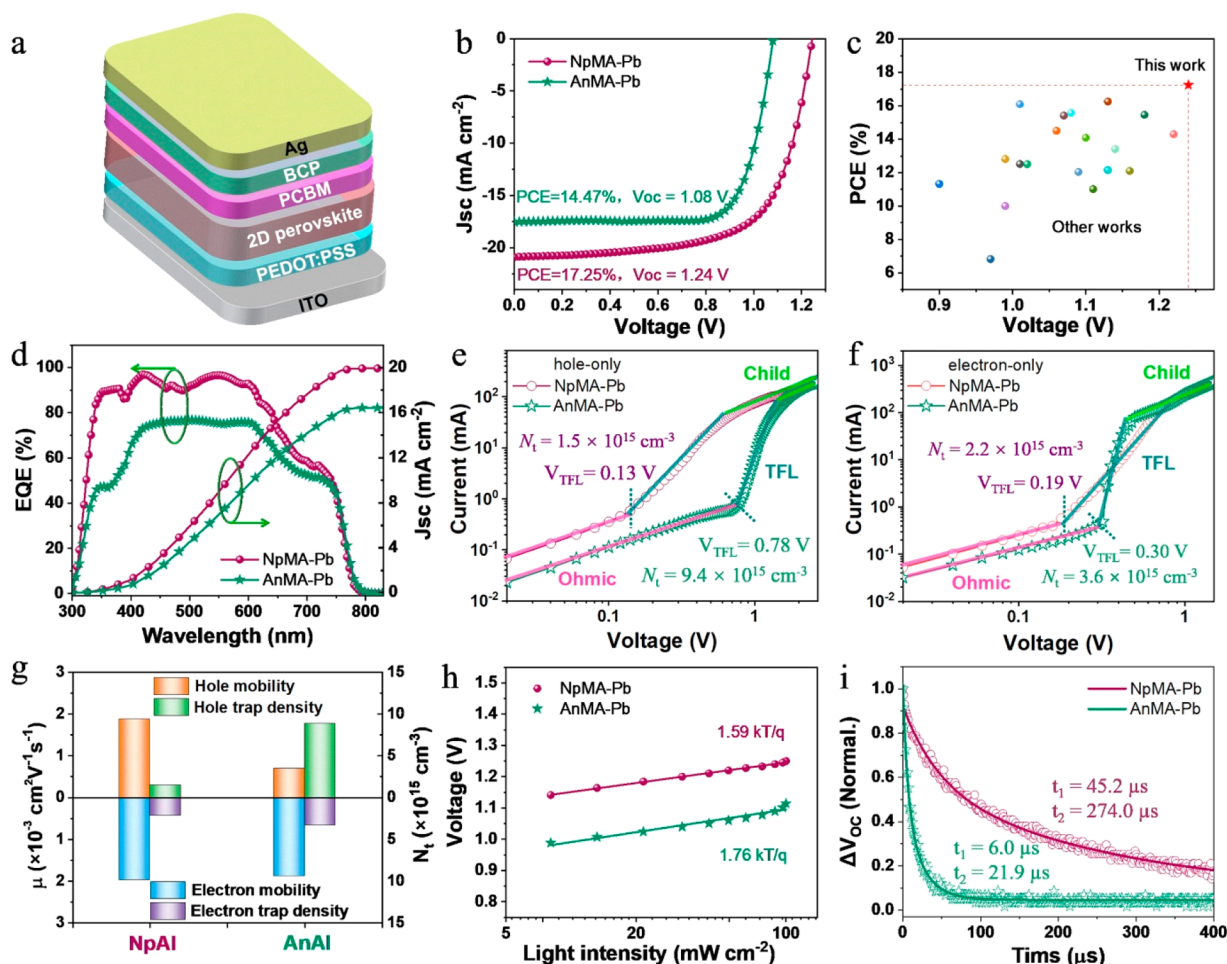


Figure 2. (a) Device structure of NpMA-Pb and AnMA-Pb PSCs. (b) J - V curves of the 2D PSCs. (c) PCE and V_{OC} of PSCs based on NpMA-Pb in comparison with published PEDOT:PSS-based 2D PSCs (average $n < 6$). (d) EQE spectra of the corresponding optimal devices. The I - V curves of (e) the hole-only device and (f) the electron-only device. (g) Calculation and statistics of trap density and mobility for the corresponding devices. (h) V_{OC} versus light intensity for the NpMA-Pb and AnMA-Pb PSCs. (i) Transient photovoltage decay curves for the NpMA-Pb and AnMA-Pb films.

vertical directions. The NpMA-Pb film exhibits a higher $I_{(202)}/I_{(111)}$ intensity ratio of 0.33 in comparison with that of 0.28 for the AnMA-Pb film, suggesting that more 2D perovskite slabs grow along vertical directions with respect to the substrate in the NpMA-Pb film.⁴² Furthermore, the (111) diffraction peak is slightly shifted to a higher angle for NpMA-Pb (14.47°) in comparison with that of AnMA-Pb (14.41°), indicating the lattice contraction of NpMA-Pb in the film due to the smaller size of NpMA.²² The scraped powder from the oriented NpMA-Pb and AnMA-Pb films exhibits obvious diffraction peaks of (0k0) as well as (111) and (202) (Figure S7b), suggesting the random orientation of 2D perovskite in the powder state. The XRD of 2D perovskite films with $n = 1$ and 2 were also exploited for comparison (Figure S8), in which the characteristic peaks of lattice planes such as (002) for $n = 1$ and (020) for $n = 2$ were observed, indicating the parallel orientation of NpMA-Pb and AnMA-Pb perovskites with an n value lower than 3. The top-view field-emission SEM image (Figure 1f) shows that the NpMA-Pb film exhibits a dense web of nanorod structure, suggesting its excellent crystallinity, which is consistent with the XRD results. The AnMA-Pb film (Figure 1g) shows a dense and compact morphology, where small size grains and a long nanorod coexist in the film. The smaller grain size for the AnMA-Pb film is in accordance with

its relatively weak diffraction peak in the XRD data. The NpMA-Pb film with nanorod-like morphology is beneficial to light absorption and charge transport compared to that of the conventional planar film, resulting in a high photovoltaic performance as discussed below.^{43,44}

Photovoltaic Performances. The photovoltaic devices were fabricated with a conventional structure of glass/ITO/PEDOT:PSS/perovskite/PCBM/BCP/Ag (Figure 2a). With a nominal n -value of 4, the 2D RP perovskites NpMA-Pb and AnMA-Pb were used as photoactive layers. The statistical photovoltaic data for devices based on these 2D RP perovskite are shown in Figure S10. As shown in Figure 2b, the device based on NpMA-Pb displays an ultrahigh V_{OC} of 1.24 V, a large short-circuit current density (J_{SC}) of 20.89 mA cm^{-2} , a fill factor (FF) of 66.35%, and an overall PCE of 17.25%, which is among the highest efficiencies so far for 2D RP PSCs ($n < 5$) to the best of our knowledge.^{25,42,45–48} While the 2D perovskite with a larger spacer, AnMA, shows a low PCE of 14.47%, coupled with a V_{OC} of 1.08 V, a J_{SC} of 17.54 mA cm^{-2} , and an FF of 76.4%. The enhanced crystallinity as evidenced by the SEM images and XRD results above should play an important role for the performance enhancement of the NpMA-Pb-based device. The PCE and V_{OC} of PSCs based on NpMA-Pb were compared with those of the published

Table 1. Optimized Device Parameters for NpMA-Pb- and AnMA-Pb-Based Devices

perovskite	V_{OC} (V)	J_{SC} (mA cm ⁻²)	FF (%)	PCE (%)	N_t^h ($\times 10^{15}$ cm ⁻³)	N_t^e ($\times 10^{15}$ cm ⁻³)	μ_h ($\times 10^{-3}$ cm ² V ⁻¹ s ⁻¹)	μ_e ($\times 10^{-3}$ cm ² V ⁻¹ s ⁻¹)	μ_h/μ_e	decay time ^b τ_1/τ_2 (ns)
NpMA-Pb ^a	1.24	20.89	66.35	17.25	1.49	2.18	1.88	1.97	1.05	104/560
AnMA-Pb ^a	1.08	17.53	76.34	14.47	8.56	3.29	0.70	1.88	2.69	59/162

^aAverage n value is 4. ^bDecay time extracted from TRPL.

PEDOT:PSS-based 2D PSCs (average $n < 6$) with inverted structure (Figure 2c), and the detailed data are presented in Table S2. As shown in Figure 2c, both the PCE and V_{OC} are the highest among the published PEDOT:PSS-based devices. Moreover, compared to AnMA-Pb, the devices based on NpMA-Pb exhibit higher V_{OC} and J_{SC} , which could be attributed to the enlarged charge carrier lifetime, reduced trap density, and decreased charge carrier nonradiative recombination loss in NpMA-Pb films as discussed below. The valence bands (VB) of NpMA-Pb and AnMA-Pb were measured and calculated from ultraviolet photoelectron spectroscopy (UPS) (Figures S11 and S12). The upshifted VB of NpMA-Pb compared to AnMA-Pb could prevent the backflow of the electron from PCBM more efficiently, thus suppressing the charge recombination.⁴⁸ Considering that the optical bandgap of the NpMA-Pb film is about 1.58 eV (Figure 1b), the energy loss of the NpMA-Pb-based device ($V_{OC} = 1.24$ V) is only 0.34 eV due to the suppressed charge carrier recombination loss and efficient charge transport. Note that the NpMA-Pb film was dominated by layered perovskite phases ($n = 2, 3, 4, 5$) with a large bandgap compared to the AnMA-Pb film as discussed below, which could also contribute to the enlarged V_{OC} .¹⁵

The external quantum efficiency (EQE) curves of the corresponding 2D RP perovskite devices are shown in Figure 2d. Compared to the AnMA-based device, the NpMA-based device shows a much higher EQE with an average value over 90% across the wavelength region from 350 to 600 nm, suggesting the excellent photon-to-current response. The dramatically reduced photoresponse for both NpMA- and AnMA-based devices over 600 nm could be ascribed to the insufficient light absorption nature of 2D RP perovskites at long wavelength, consistent with their absorption spectra. The integrated J_{SC} are 19.94 and 16.43 mA cm⁻² for NpMA-Pb- and AnMA-Pb-based devices, respectively, which are less than 5% mismatch with respect to the J_{SC} obtained from $J-V$ curves. Compared to the control 3D MAPbI₃ perovskite with the same device structure,²³ both NpMA-Pb and AnMA-Pb devices show reduced hysteresis (Figure S13 and Table S3), which could be attributed to the hindered ion motion due to the large-size organic spacer used in the films. After illuminating under 1 sun for 150 s by holding the voltage at the maximum power point (Figure S14), the stabilized PCEs of 16.8% and 13.2% were achieved for NpMA-Pb- and AnMA-Pb-based devices, respectively, which are matched well with the $J-V$ measurements.

Charge Carrier Dynamics. The trap density of electrons and holes was further evaluated to better understand the charge carrier dynamics of NpMA- and AnMA-based 2D perovskite films. Hole-only devices with the structure of ITO/PEDOT:PSS/perovskite/Spiro-OMeTAD/MoO₃/Ag and electron-only devices with the structure of ITO/SnO₂/perovskite/PCBM/BCP/Ag were fabricated (Figure 2e,f). The trap density (N_t) was calculated by the trap-filled limit

voltage (V_{TFL}) using the equation $N_t = 2\epsilon_0\epsilon_r V_{TFL}/qL^2$, where ϵ_r is the relative dielectric constant ($\epsilon_r = 25$),⁴⁹ ϵ_0 is the vacuum permittivity, q is the elemental charge, and L is the thickness of the 2D RP perovskite films. The NpMA-Pb film exhibits a lower trap density of 1.49×10^{15} cm⁻³ for the hole and 2.18×10^{15} cm⁻³ for the electron in comparison with the AnMA-Pb film (8.56×10^{15} cm⁻³ for a hole and 3.29×10^{15} cm⁻³ for an electron), as shown in Figure 2e,f. The lower hole and electron trap state density is expected to reduce the charge recombination and benefit charge transport, which is consistent with the enhanced and balanced mobility for the NpMA-Pb film as shown in Figure 2g and Table 1.

To understand the charge carrier recombination losses in the NpMA-Pb- and AnMA-Pb-based devices during device operation, the light intensity dependent $J-V$ characteristics were investigated. The J_{SC} versus light intensity ($J \propto I^{\alpha}$) in a double logarithmic scale (Figure S15a) shows that the NpMA-Pb-based device exhibits an α value of 0.999, suggesting its lower nongeminate recombination than that of an AnMA-Pb ($\alpha = 0.967$)-based device.⁵⁰ Figure 2h shows a linear fitting of V_{OC} versus the natural logarithm of light intensity. Both devices exhibit a strong dependence of V_{OC} on the light intensity, with a slope of $1.59 kT/q$ for NpMA-Pb- and $1.76 kT/q$ for AnMA-Pb-based devices, where k is Boltzmann's constant, T is temperature, and q is elementary charge. The lower slope for the NpMA-Pb-based device indicates the reduced trap-assisted recombination, which could be ascribed to the enhanced crystallinity of the NpMA-Pb film with decreased trap density, resulting in enlarged V_{OC} and better device performance.

To investigate the charge recombination process in NpMA-Pb- and AnMA-Pb based devices under operating conditions, transient photovoltage (TPV) measurements were conducted.⁵¹ As shown in Figure 2i, the lifetime of the NpMA-Pb-based device is 45.2 μ s, which is much larger than that of the AnMA-Pb-based device (6 μ s), indicating the reduced nonradiative recombination and the enhanced carrier lifetime in the NpMA-Pb-based device, in good agreement with the PL and TRPL measurements discussed above. Meanwhile, the photocurrent decay time of the NpMA-Pb-based device is shorter than that of the AnMA-Pb-based device (Figure S15b), suggesting more efficient charge collection in the NpMA-based device.

The grazing incidence wide-angle X-ray scattering (GI-WAXS) analysis was performed to probe more information about crystal orientation and phase dispersity of 2D perovskite films as shown in Figure 3a,b. The NpMA-Pb film exhibits stronger, sharper, and more discrete Bragg spots than that of the AnMA-Pb film, especially for the (111) and (202) planes, which indicates that the layered perovskite phases prefer to be orientated vertical to the substrate in the NpMA-Pb film, as illustrated in Figure 3c.¹⁶ This vertical crystal orientation would facilitate the efficient charge transport between the top and bottom electrodes and enhance the photovoltaic performance of 2D PSCs. As shown in Figure 3b, the AnMA-Pb film

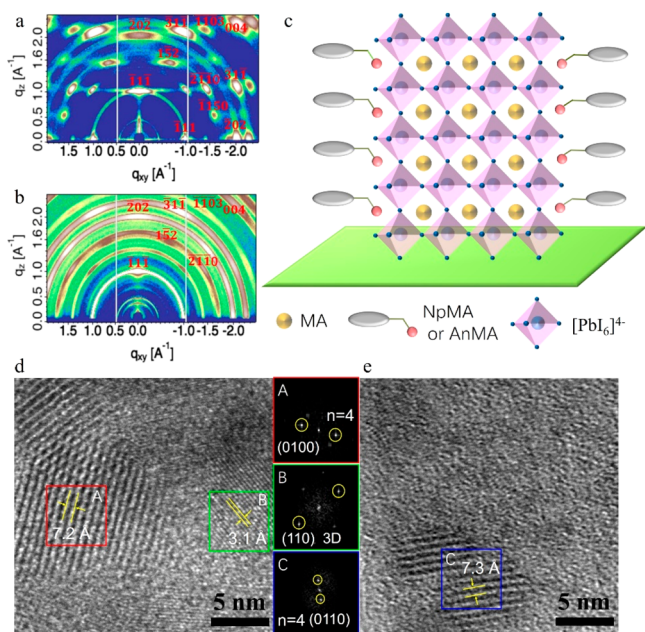


Figure 3. (a) GIWAXS patterns of the NpMA-Pb film. (b) GIWAXS patterns of the AnMA-Pb film. (c) Schematic illustration of the proposed 2D perovskite structure. (d) HRTEM image of the NpMA-Pb film. (e) HRTEM image of the AnMA-Pb film. Insets: Fast Fourier transforms (FFT) of the selected area diffraction.

also exhibits obvious Bragg diffraction spots of the (111) and (202) plane, which coexist with the diffraction rings, suggesting the disorder distribution of layered perovskite in the AnMA-Pb film.⁵² Moreover, diffraction dots at $q < 1.0 \text{ \AA}^{-1}$ were observed for both NpMA-Pb and AnMA-Pb films, which were 2D

perovskite phases with an n value lower than 4,³⁷ further suggesting that the films are composed of multiple perovskite phases with different n values.

The HRTEM and the fast Fourier transforms (FFT) analysis were conducted to study the phase distribution in 2D RP perovskite films. As shown in Figure 3d, a lattice spacing of 7.2 Å can be found in region A, which corresponds to the diffraction of the (0100) plane for the $n = 4$ phase in the NpMA-Pb film (Table S4, Supporting Information). The narrower lattice spacing of 3.1 Å in region B can be assigned to the (110) diffraction of MAPbI₃.⁵³ Meanwhile, the lattice spacings of 3.6 and 7.9 Å corresponding to the (0100) diffraction ($n = 1$) and the (060) diffraction ($n = 2$), respectively, were also found in the NpMA-Pb film (Figure S16a and Table S4). Accordingly, a lattice spacing of 7.3 Å in Figure 3e can be discovered to match with the diffraction of (0110) ($n = 4$) for AnMA-Pb perovskites, and the weak 2D phase with $n = 1$ and $n = 2$ can also be found in the HRTEM of the AnMA-Pb film (Figure S16b and Table S5). The simplified schematic illustration of the crystal structures of NpMA-Pb and AnMA-Pb perovskites is shown in Figure S17. These results clearly verify that multiple phases, including different layered perovskite phases and 3D or 3D-like phases, coexist and distribute randomly in both NpMA-Pb and AnMA-Pb films, which could be ascribed to the differences in the thermodynamic stability of 2D perovskite phases with large n -values.⁵⁴

To have a better understanding of the working principle of 2D RP PSCs, we performed ultrafast TA spectroscopy to probe the phase compositions and the charge-transfer dynamics in the NpMA- and AnMA-based 2D perovskites. The samples were excited from the back side (glass side) (Figure 4a–f) with a 400 nm pump beam ($20 \mu\text{J cm}^{-2}$) by a femtosecond laser pulse, and then the white light probe pulse generated by the

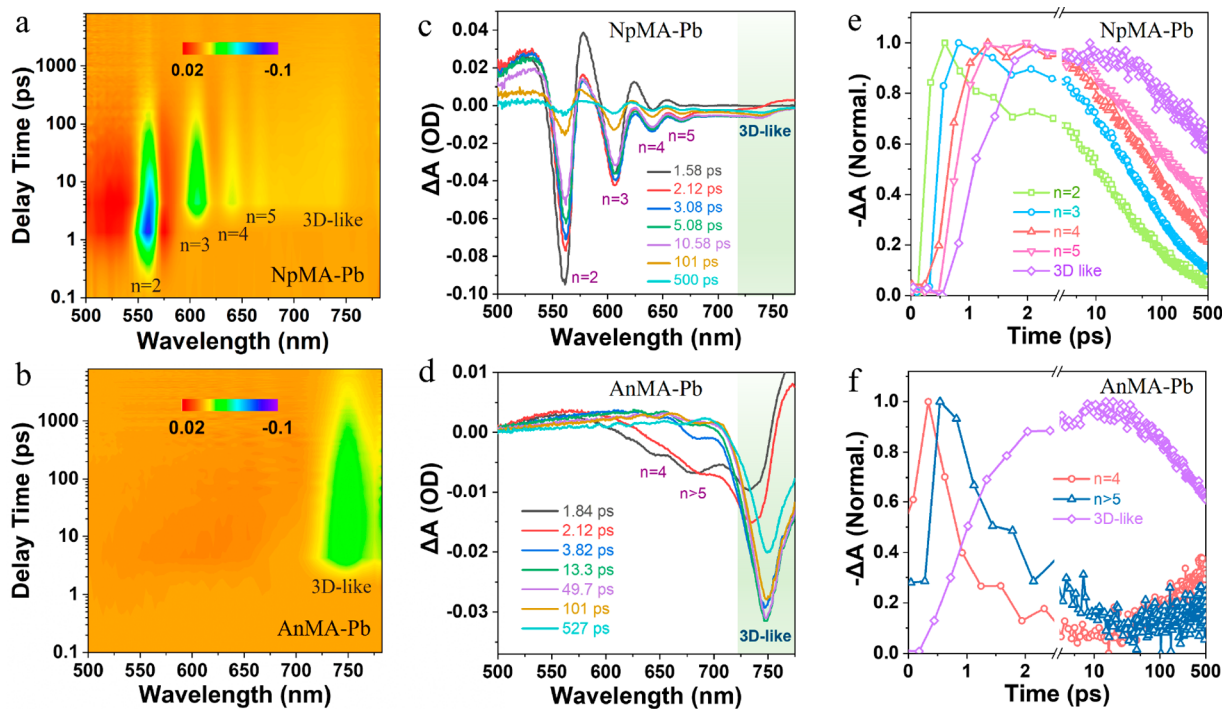


Figure 4. Time- and wavelength-dependent TA images of the NpMA-Pb film (a) and the AnMA-Pb film (b). TA spectra at selected probe times of the NpMA-Pb film (c) and the AnMA-Pb film (d). TA spectra for different n phases as a function of delay time of the NpMA-Pb film (e) and the AnMA-Pb film (f).

time-lapse laser is used to detect changes in the light absorption (ΔA) spectrum.⁵⁵ The exciton accumulation at different delay times can be monitored by the ground-state bleach (GSB) due to the charge filling, and the exciton absorption of various 2D perovskite phases display clear GSB signals.³⁸ As shown in Figure 4a, the NpMA-Pb film features clear and strong GSB signals at ~ 561 , 606, and 640 nm, which can be assigned to the phases with $n = 2, 3$, and 4. The weak GSB signals at ~ 667 and 740 nm can be assigned to the $n = 5$ phase and 3D-like phase, respectively. These results confirmed that the NpMA-Pb film exhibited multiple layered perovskite phases with different n -values and low n -value 2D phases dominated in the NpMA-Pb film, which is consistent with the absorption spectra and PL and HRTEM results discussed above. Conversely, as shown in Figure 4b, the AnMA-Pb film only exhibits strong GSB signals at ~ 750 nm, suggesting the 3D-like phases dominated in the perovskite film.

The TA spectra at different delay times are shown in Figure 4c for the NpMA-Pb film and Figure 4d for the AnMA-Pb film. The NpMA-Pb film exhibits diverse GSB peaks, which can be assigned to identical phases appearing at the same wavelengths shown in Figure 4a. It reflects a bleach decay at $n = 2, 3, 4$, and 5 phase, and this process was accompanied by the formation of 3D-like phases with increasing delay time. As shown in Figure 4d, GSB peaks at ~ 645 and ~ 682 nm can be assigned to $n = 4$ and $n > 5$ phases. Simultaneously, the broad GSB peak, which is related to 3D-like phases, is red-shifted from 732 nm at 1.84 ps to 750 nm at 527 ps with the increasing delay time, suggesting the formation of closely separated energy levels.^{56,57}

The TA kinetics of different 2D perovskite phases probed at the corresponding GSB peaks are shown in Figure 4e,f. For the NpMA-Pb film, the excitons are primarily created in the 2D phases with $n = 2, 3, 4$, and 5 within 1.3 ps. Following the fast buildup, the bleaching of 2D phases with $n = 2, 3, 4$, and 5 shows ultrafast decay times of $\tau_1 = 0.56, 1.01, 4.64$, and 5.07 ps, in accordance with the rapid bleaching rise of 3D-like phases within a time constant of $\tau_{\text{et}} = 6.56$ ps, suggesting ultrafast energy transfer (or exciton transfer) accomplished in picoseconds.³⁸ These results indicate that the photogenerated excitons in low n value phases could be localized to 3D-like phases within 7 ps.³² For the AnMA-Pb film, as shown in Figure 4f, the excitons are primarily created in the $n = 4$ and >5 phases with weak GSB signal, and the bleaching decay time is well matched with the fast bleaching formation time of the 3D-like phase ($\tau_{\text{et}} = 10.17$ ps). The longer bleaching formation time of the 3D-like phase in the AnMA-Pb film compared to that of the NpMA-Pb film indicates more efficient and faster exciton transfer from layer phases to 3D-like phases in the NpMA-Pb film. All above results indicate that the exciton transfer from a wide-bandgap layered perovskite (small n phases) to 3D-like phases occurs on the picosecond time scale.⁵⁸ In the AnMA-Pb film, low n -value phases ($n < 4$) were scarcely formed, and it failed to accumulate photogenerated excitons, leading to inefficient energy transfer.⁵⁶ Notably, the energy transfer could be facilitated by the shorter spacing cation,⁵⁹ and the closely separated energy levels of the NpMA-Pb film may lead to a more efficient energy transfer route in comparison with the AnMA-Pb film.⁵⁶

The TA spectra (Figure 4a,c) show that the NpMA-Pb film exhibits obviously layered perovskite phases from 2 to 5 but weak 3D-like phases, indicating the low n -value 2D perovskite phases dominate in the NpMA-Pb film. On the contrary, as shown in Figure 4b,d, the 3D-like phase dominated in the

AnMA-Pb film. However, the device based on the NpMA-Pb film with dominated layered perovskite phases, in which the exciton binding energy is very high and difficult to separate at room temperature,³⁵ shows higher photovoltaic performance compared to the AnMA-Pb-based device. The results suggest that the exciton separation and transport channels are mainly located in 3D-like phases, and the weak 3D-like perovskite phase plays the major role for exciton separation and transportation in the NpMA-Pb film. This exciton transport and separation mechanism is further supported by the phase distribution shown in HRTEM images, where multiple low n value layered perovskite phases and 3D-like perovskites coexist and distribute randomly. Meanwhile, the PL and TA measured through back and front sides show similar characteristics (Figure S6 and Figure S18), further verifying the random dispersion of different- n -value phases.

On the basis of the above analysis, as shown in Figure 5, we propose that the photogenerated excitons in the 2D perovskite

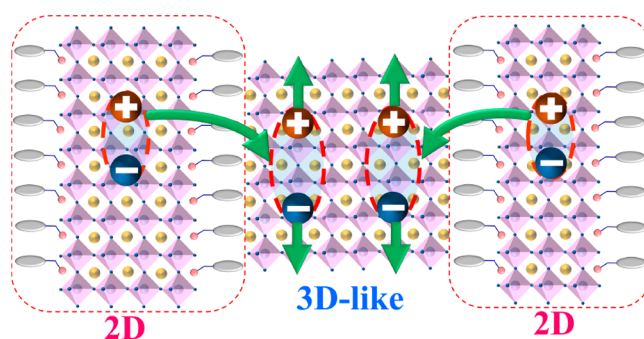


Figure 5. Schematic diagram of exciton migration dynamics for 2D perovskite film.

film would migrate from low- n phase to adjacent 3D-like phase in picoseconds and then dissociate into free charge carrier quickly due to the weak exciton binding energy in the 3D-like perovskite. The ultrafast exciton migration between layered 2D perovskite phases and 3D-like phases resulting from energy transfer is responsible for the high photovoltaic performance of 2D perovskite devices. Note that more 3D-like phases could not guarantee higher photovoltaic performance because other factors, such as phase distribution, crystal orientation, and trap density, also have effects on the photovoltaic performance of the devices.

Film and Device Stability. The stability of devices against light, humidity, and heat is a key factor for their development and commercialization, so the stability tests under various conditions of NpMA-Pb and AnMA-Pb PSCs were assessed against the control device based on MAPbI₃. The water contact angles of NpMA-Pb, AnMA-Pb, and MAPbI₃ films are 82.77°, 76.62°, and 43.32°, respectively. The enlarged water contact angle for NpMA-Pb film could prevent water-induced degradation and improve the moisture stability of the film (Figure S19). The XRD measurements were further conducted to investigate moisture stability under $45 \pm 5\%$ relative humidity (RH) conditions with different storage times for NpMA-Pb, AnMA-Pb, and MAPbI₃ films (Figure 6a–c). The control MAPbI₃ film was completely degraded to PbI₂ after storage for 240 h, confirmed by a sharp peak at about 12.7° in the XRD pattern. By contrast, there are no PbI₂ peaks observed even after 480 h for NpMA-Pb and AnMA-Pb films. The results indicate that NpMA-Pb and AnMA-Pb films exhibit

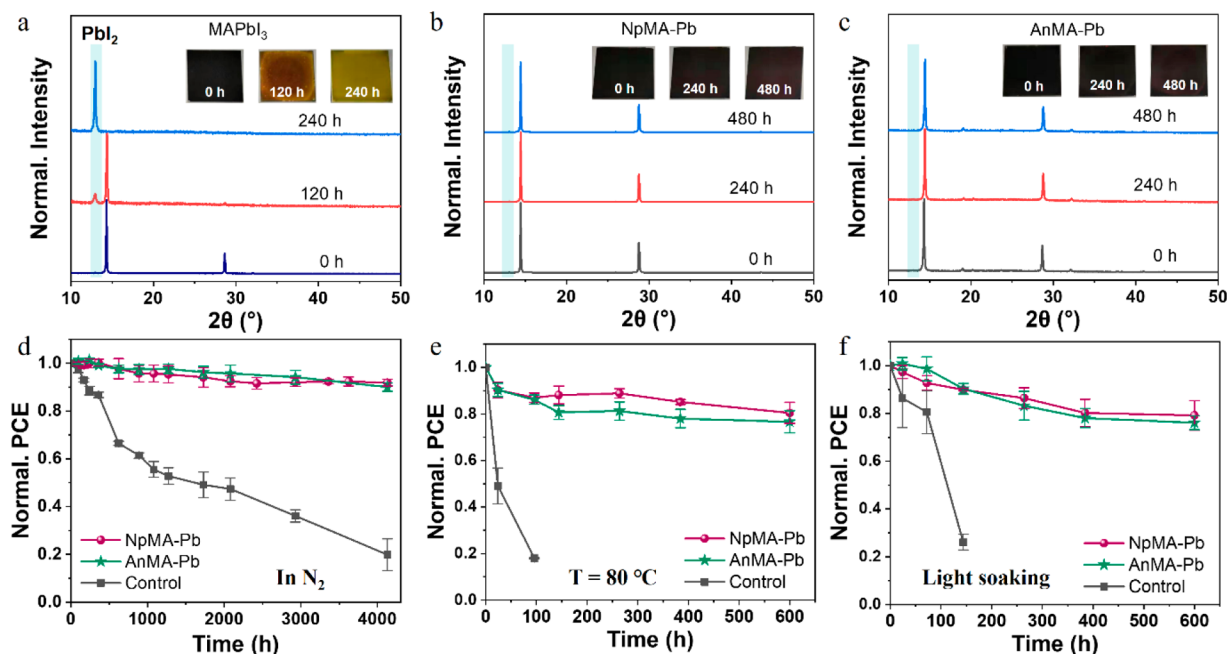


Figure 6. XRD patterns of MAPbI₃ (a), NpMA-Pb (b), and AnMA-Pb (c) films exposed in ambient air with an RH of 40–50% for 0 h, 240, and 480 h. (d–f) Normalized photovoltaic parameters versus time for unencapsulated 2D and control 3D perovskite device storage in N₂ at room temperature (d), at 80 °C (e), and under continuous light soaking (100 mW cm⁻²) at room temperature (f).

excellent environment stability in comparison with that of the control 3D perovskite film owing to their inherent hydrophobic property as discussed above.

We further investigated long-term stability of unencapsulated devices stored in N₂ at room temperature (RT). As shown in Figure 6d and Figure S20, the 2D RP perovskite devices show greatly enhanced stability compared to the control device. The NpMA-Pb and AnMA-Pb PSCs retained an average of 91% and 90% of their initial PCEs after 4100 h (over 170 days), while the control device only retained 20% of its original PCE. The results are consistent with moisture stability data measured in ambient conditions with 30 ± 5% RH (Figure S21), where NpMA-Pb and AnMA-Pb perovskite devices without encapsulation maintained 89% and 80% of their initial PCEs after 1000 h, while the control device only retained 24% of its initial PCE. Furthermore, the thermal stability of unencapsulated devices was measured in N₂ at 80 °C as shown in Figure 6e and Figure S22. The NpMA-Pb and AnMA-Pb PSCs retained 80% and 77% of their original PCEs after 600 h, whereas the control device degraded to ~18% of the initial PCE after 96 h. Light stability data of the devices measured in N₂ under continuous light illumination (white-light-emitting diode (LED), 100 mW cm⁻²) are shown in Figure 6f and Figure S23. The PCEs of NpMA-Pb- and AnMA-Pb-based devices remained 79% and 76% of their initial PCEs after 600 h, while MAPbI₃ PSCs only retained 26% of their initial PCEs after 144 h. These enhanced device stabilities could be attributed to the intrinsic stability of 2D RP perovskites by incorporated multiple-ring aromatic organic spacers with superior hydrophobic and high thermal stability, which stress the importance of the development of organic spacers for 2D RP perovskites.

CONCLUSIONS

In conclusion, a class of multiple-ring aromatic spacers (NpMA and AnMA) has been developed for 2D RP PSCs, and high

photovoltaic performance has been demonstrated. With a nominal $n = 4$ average composition, NpMA-based devices exhibit a high V_{OC} of 1.24 V and a champion PCE of 17.25%, which is among the highest efficiencies for 2D RP PSCs ($n < 5$) to the best of our knowledge. Dramatically improved storage stability was realized with retaining an average 91% of their initial efficiency after 4100 h (over 170 days) and maintaining 79% under continuous light soaking after 600 h. The HRTEM images show that the 2D layered phases and 3D-like phases coexist and are randomly distributed in the 2D RP perovskite film. An important finding is that the NpMA-Pb film with dominant layered perovskite phases exhibits much higher photovoltaic efficiency compared to the AnMA-Pb film due to the ultrafast exciton migration (within 7 ps) from 2D layered phases to 3D-like phases, resulting in efficient exciton separation, charge transportation, and collection. We believe that our findings would help to understand the working mechanism of 2D PSCs in-depth and offer an efficient way to further boost their efficiency and stability toward future industry applications.

EXPERIMENTAL SECTION

Preparation of the 2D RP Perovskite Precursor Solution.

The 2D perovskite (NpMA)₂(MA)₃Pb₄I₁₃ and (AnMA)₂(MA)₃Pb₄I₁₃ (the concentration of Pb²⁺ is 1 M in DMF) precursor solutions were prepared by mixing NpMAI (or AnMAI), MAI, and PbI₂ in a stoichiometric ratio of 2:3:4 in DMF. MAI was added to the precursor solution with a MAI/MAI weight ratio of 0.5:1. The solutions were stirred at 70 °C for 12 h and cooled to room temperature before use.

Device Fabrication and Characterization. The ITO-coated glasses were cleaned sequentially in distilled water, acetone, and isopropyl alcohol two times. The ITO substrates were treated with UV-ozone for 15 min before spin coating of a layer of PEDOT:PSS (Baytron P VP AI 4083) at 4000 rpm for 20 s as hole-transport material and then annealed at 150 °C for 15 min in air. Then the substrates were transferred to a nitrogen glovebox. The 2D perovskite precursors were then spin-coated on top of the ITO/PEDOT:PSS

substrates at 8000 rpm for 90 s. Two-hundred microliters of anisole antisolvent was dropped on the perovskite films twice at 60 and 20 s before the end of the procedure. Then the as-fabricated films were annealed at 100 °C for 40 min in air. The PC₆₁BM solution (30 μL, 20 mg/mL in CB) as electron-transport material was formed by spin-coating the precursor on top of the films at 1500 rpm for 40 s. After that, the solution of BCP (0.6 mg/mL in isopropyl alcohol) was spin-coated on top of PC₆₁BM at 1000 rpm for 60 s. Finally, the thermal evaporation of 80 nm of Ag as electrode was conducted under a vacuum of 1×10^{-4} Pa. The effective area was 10 mm² defined by a mask.

ASSOCIATED CONTENT

Supporting Information

The Supporting Information is available free of charge at <https://pubs.acs.org/doi/10.1021/acsnano.0c00875>.

Experimental details and additional characterizations; materials synthesis, device fabrication, and characterization details; ¹H NMR spectra, XPS spectra, UV–vis absorption spectra, PL, XRD, cross-section SEM, UPS, light intensity dependence, HRTEM, TA spectra, water contact angle, *J*–*V* curves of device stability measurements; tables showing TRPL parameters, summary of *V*_{OC} and PCEs of PEDOT:PSS-based 2D RP PSCs, photovoltaic parameters of Figure S13, calculated *d* spacing values, and fitted parameters for the TA kinetics from Figure S18c,f (PDF)

AUTHOR INFORMATION

Corresponding Author

Yongsheng Liu – *The Centre of Nanoscale Science and Technology and Key Laboratory of Functional Polymer Materials, Institute of Polymer Chemistry, College of Chemistry and Renewable Energy Conversion and Storage Center (RECAST), Nankai University, Tianjin 300071, China;* orcid.org/0000-0002-7135-723X; Email: liuys@nankai.edu.cn

Authors

Zhiyuan Xu – *The Centre of Nanoscale Science and Technology and Key Laboratory of Functional Polymer Materials, Institute of Polymer Chemistry, College of Chemistry, Nankai University, Tianjin 300071, China*

Di Lu – *The Centre of Nanoscale Science and Technology and Key Laboratory of Functional Polymer Materials, Institute of Polymer Chemistry, College of Chemistry, Nankai University, Tianjin 300071, China*

Feng Liu – *Department of Polymer Science and Engineering, School of Chemistry and Chemical Engineering, Shanghai Jiao Tong University, Shanghai 200240, China*

Hongtao Lai – *The Centre of Nanoscale Science and Technology and Key Laboratory of Functional Polymer Materials, Institute of Polymer Chemistry, College of Chemistry, Nankai University, Tianjin 300071, China*

Xiangjian Wan – *The Centre of Nanoscale Science and Technology and Key Laboratory of Functional Polymer Materials, Institute of Polymer Chemistry, College of Chemistry and Renewable Energy Conversion and Storage Center (RECAST), Nankai University, Tianjin 300071, China*

Xiaodan Zhang – *Institute of Photoelectronic Thin Film Devices and Technology and Renewable Energy Conversion and Storage Center (RECAST), Nankai University, Tianjin 300071, China;* orcid.org/0000-0002-0522-5052

Yongsheng Chen – *The Centre of Nanoscale Science and Technology and Key Laboratory of Functional Polymer Materials, Institute of Polymer Chemistry, College of Chemistry and Renewable Energy Conversion and Storage Center (RECAST), Nankai University, Tianjin 300071, China;* orcid.org/0000-0003-1448-8177

Complete contact information is available at: <https://pubs.acs.org/doi/10.1021/acsnano.0c00875>

Notes

The authors declare no competing financial interest.

ACKNOWLEDGMENTS

This work was financially supported by the National Natural Science Foundation of China (Grants Nos. 21875122, 51673097) and the Fundamental Research Funds for the Central Universities.

REFERENCES

- Grätzel, M. The Rise of Highly Efficient and Stable Perovskite Solar Cells. *Acc. Chem. Res.* **2017**, *50*, 487–491.
- Correa-Baena, J. P.; Saliba, M.; Buonassisi, T.; Grätzel, M.; Abate, A.; Tress, W.; Hagfeldt, A. Promises and Challenges of Perovskite Solar Cells. *Science* **2017**, *358*, 739–744.
- Green, M. A.; Ho-Baillie, A.; Snaith, H. J. The Emergence of Perovskite Solar Cells. *Nat. Photonics* **2014**, *8*, 506–514.
- Kojima, A.; Teshima, K.; Shirai, Y.; Miyasaka, T. Organometal Halide Perovskites as Visible-Light Sensitizers for Photovoltaic Cells. *J. Am. Chem. Soc.* **2009**, *131*, 6050–6051.
- Kim, H. S.; Lee, C. R.; Im, J. H.; Lee, K. B.; Moehl, T.; Marchioro, A.; Moon, S. J.; Humphry-Baker, R.; Yum, J. H.; Moser, J. E.; Grätzel, M.; Park, N. G. Lead Iodide Perovskite Sensitized All-Solid-State Submicron Thin Film Mesoscopic Solar Cell with Efficiency Exceeding 9%. *Sci. Rep.* **2012**, *2*, 591–597.
- Yang, W. S.; Park, B. W.; Jung, E. H.; Jeon, N. J.; Kim, Y. C.; Lee, D. U.; Shin, S. S.; Seo, J.; Kim, E. K.; Noh, J. H.; Seok, S. I. Iodide Management in Formamidinium-Lead-Halide-Based Perovskite Layers for Efficient Solar Cells. *Science* **2017**, *356*, 1376–1379.
- Jiang, Q.; Zhao, Y.; Zhang, X. W.; Yang, X. L.; Chen, Y.; Chu, Z. M.; Ye, Q. F.; Li, X. X.; Yin, Z. G.; You, J. B. Surface Passivation of Perovskite Film for Efficient Solar Cells. *Nat. Photonics* **2019**, *13*, 460–466.
- NREL. Best Research-Cell Efficiencies. <https://www.nrel.gov/pv/cell-efficiency.html> (accessed: March 14, 2020).
- Yang, S.; Chen, S.; Mosconi, E.; Fang, Y.; Xiao, X.; Wang, C.; Zhou, Y.; Yu, Z.; Zhao, J.; Gao, Y.; De Angelis, F.; Huang, J. Stabilizing Halide Perovskite Surfaces for Solar Cell Operation with Wide-Bandgap Lead Oxysalts. *Science* **2019**, *365*, 473–478.
- Tress, W.; Domanski, K.; Carlsen, B.; Agarwalla, A.; Alharbi, E. A.; Graetzel, M.; Hagfeldt, A. Performance of Perovskite Solar Cells under Simulated Temperature-Illumination Real-World Operating Conditions. *Nat. Energy* **2019**, *4*, 568–574.
- Hou, Y.; Du, X.; Scheiner, S.; McMeekin, D. P.; Wang, Z.; Li, N.; Killian, M. S.; Chen, H.; Richter, M.; Levchuk, I.; Schrenker, N.; Spiecker, E.; Stubhan, T.; Luechinger, N. A.; Hirsch, A.; Schmuki, P.; Steinrueck, H. P.; Fink, R. H.; Halik, M.; Snaith, H. J.; et al. A Generic Interface to Reduce the Efficiency-Stability-Cost Gap of Perovskite Solar Cells. *Science* **2017**, *358*, 1192–1197.
- Matteocci, F.; Cinà, L.; Lamanna, E.; Cacovich, S.; Divitini, G.; Midgley, P. A.; Ducati, C.; Di Carlo, A. Encapsulation for Long-Term Stability Enhancement of Perovskite Solar Cells. *Nano Energy* **2016**, *30*, 162–172.
- Chao, L.; Xia, Y.; Li, B.; Xing, G.; Chen, Y.; Huang, W. Room-Temperature Molten Salt for Facile Fabrication of Efficient and Stable Perovskite Solar Cells in Ambient Air. *Chem.* **2019**, *5*, 995–1006.

- (14) Mao, L. L.; Stoumpos, C. C.; Kanatzidis, M. G. Two-Dimensional Hybrid Halide Perovskites: Principles and Promises. *J. Am. Chem. Soc.* **2019**, *141*, 1171–1190.
- (15) Quan, L. N.; Yuan, M.; Comin, R.; Voznyy, O.; Beauregard, E. M.; Hoogland, S.; Buin, A.; Kirmani, A. R.; Zhao, K.; Amassian, A.; Kim, D. H.; Sargent, E. H. Ligand-Stabilized Reduced-Dimensionality Perovskites. *J. Am. Chem. Soc.* **2016**, *138*, 2649–2655.
- (16) Tsai, H.; Nie, W.; Blancon, J. C.; Toumpos, C. C. S.; Asadpour, R.; Harutyunyan, B.; Neukirch, A. J.; Verduzco, R.; Crochet, J. J.; Tretiak, S.; Pedesseau, L.; Even, J.; Alam, M. A.; Gupta, G.; Lou, J.; Ajayan, P. M.; Bedzyk, M. J.; Kanatzidis, M. G.; Mohite, A. D. High-Efficiency Two-Dimensional Ruddlesden-Popper Perovskite Solar Cells. *Nature* **2016**, *536*, 312–316.
- (17) Calabrese, J.; Jones, N. L.; Harlow, R. L.; Herron, N.; Thorn, D. L.; Wang, Y. Preparation and Characterization of Layered Lead Halide Compounds. *J. Am. Chem. Soc.* **1991**, *113*, 2328–2330.
- (18) Zhang, X.; Ren, X.; Liu, B.; Munir, R.; Zhu, X.; Yang, D.; Li, J.; Liu, Y.; Smilgies, D. M.; Li, R.; Yang, Z.; Niu, T.; Wang, X.; Amassian, A.; Zhao, K.; Liu, S. Stable High Efficiency Two-Dimensional Perovskite Solar Cells via Cesium Doping. *Energy Environ. Sci.* **2017**, *10*, 2095–2102.
- (19) Wang, Z.; Lin, Q.; Chmiel, F. P.; Sakai, N.; Herz, L. M.; Snaith, H. J. Efficient Ambient-Air-Stable Solar Cells with 2D–3D Heterostructured Butylammonium-Cesium-Formamidinium Lead Halide Perovskites. *Nat. Energy* **2017**, *2*, 1–10.
- (20) Chen, Y. N.; Sun, Y.; Peng, J. J.; Zhang, W.; Su, X. J.; Zheng, K. B.; Pullerits, T.; Liang, Z. Q. Tailoring Organic Cation of 2D Air-Stable Organometal Halide Perovskites for Highly Efficient Planar Solar Cells. *Adv. Energy Mater.* **2017**, *7*, 1700162.
- (21) Cheng, P.; Xu, Z.; Li, J.; Liu, Y.; Fan, Y.; Yu, L.; Smilgies, D. M.; Müller, C.; Zhao, K.; Liu, S. F. Highly Efficient Ruddlesden-Popper Halide Perovskite $\text{PA}_2\text{MA}_4\text{Pb}_5\text{I}_{16}$ Solar Cells. *ACS Energy Lett.* **2018**, *3*, 1975–1982.
- (22) Yan, Y.; Yu, S.; Honarfar, A.; Pullerits, T.; Zheng, K.; Liang, Z. Benefiting from Spontaneously Generated 2D/3D Bulk-Heterojunctions in Ruddlesden-Popper Perovskite by Incorporation of S-Bearing Spacer Cation. *Adv. Sci.* **2019**, *6*, 1900548.
- (23) Lai, H.; Kan, B.; Liu, T.; Zheng, N.; Xie, Z.; Zhou, T.; Wan, X.; Zhang, X.; Liu, Y.; Chen, Y. Two-Dimensional Ruddlesden-Popper Perovskite with Nanorod-Like Morphology for Solar Cells with Efficiency Exceeding 15%. *J. Am. Chem. Soc.* **2018**, *140*, 11639–11646.
- (24) Zhang, F.; Kim, D. H.; Lu, H. P.; Park, J. S.; Larson, B. W.; Hu, J.; Gao, L. G.; Xiao, C. X.; Reid, O. G.; Chen, X. H.; Zhao, Q.; Ndione, P. F.; Berry, J. J.; You, W.; Walsh, A.; Beard, M. C.; Zhu, K. Enhanced Charge Transport in 2D Perovskites via Fluorination of Organic Cation. *J. Am. Chem. Soc.* **2019**, *141*, 5972–5979.
- (25) Zhang, J.; Qin, J.; Wang, M.; Bai, Y.; Zou, H.; Keum, J. K.; Tao, R.; Xu, H.; Yu, H.; Haacke, S.; Hu, B. Uniform Permutation of Quasi-2D Perovskites by Vacuum Poling for Efficient, High-Fill-Factor Solar Cells. *Joule* **2019**, *3*, 3061–3071.
- (26) Niu, T.; Ren, H.; Wu, B.; Xia, Y.; Xie, X.; Yang, Y.; Gao, X.; Chen, Y.; Huang, W. Reduced-Dimensional Perovskite Enabled by Organic Diamine for Efficient Photovoltaics. *J. Phys. Chem. Lett.* **2019**, *10*, 2349–2356.
- (27) Li, P.; Liang, C.; Liu, X. L.; Li, F.; Zhang, Y.; Liu, X. T.; Gu, H.; Hu, X.; Xing, G.; Tao, X.; Song, Y. Low-Dimensional Perovskites with Diammonium and Monoammonium Alternant Cations for High-Performance Photovoltaics. *Adv. Mater.* **2019**, *31*, 1901966.
- (28) Mitzi, D. B.; Chondroudis, K.; Kagan, C. R. Design, Structure, and Optical Properties of Organic-Inorganic Perovskites Containing an Oligothiophene Chromophore. *Inorg. Chem.* **1999**, *38*, 6246–6256.
- (29) Chondroudis, K.; Mitzi, D. B. Electroluminescence from an Organic-Inorganic Perovskite Incorporating a Quaterthiophene Dye within Lead Halide Perovskite Layers. *Chem. Mater.* **1999**, *11*, 3028–3030.
- (30) Braun, M.; Tuffentsammer, W.; Wachtel, H.; Wolf, H. C. Tailoring of Energy Levels in Lead Chloride Based Layered Perovskites and Energy Transfer between the Organic and Inorganic Planes. *Chem. Phys. Lett.* **1999**, *303*, 157–164.
- (31) Du, K. Z.; Tu, Q.; Zhang, X.; Han, Q. W.; Liu, J.; Zauscher, S.; Mitzi, D. B. Two-Dimensional Lead(II) Halide-Based Hybrid Perovskites Templated by Acene Alkylamines: Crystal Structures, Optical Properties, and Piezoelectricity. *Inorg. Chem.* **2017**, *56*, 9291–9302.
- (32) Wang, N.; Cheng, L.; Ge, R.; Zhang, S.; Miao, Y.; Zou, W.; Yi, C.; Sun, Y.; Cao, Y.; Yang, R.; Wei, Y.; Guo, Q.; Ke, Y.; Yu, M.; Jin, Y.; Liu, Y.; Ding, Q.; Di, D.; Yang, L.; Xing, G.; et al. Perovskite Light-Emitting Diodes Based on Solution-Processed Self-Organized Multiple Quantum Wells. *Nat. Photonics* **2016**, *10*, 699–704.
- (33) Zhao, B.; Bai, S.; Kim, V.; Lamboll, R.; Shivanna, R.; Auras, F.; Richter, J. M.; Yang, L.; Dai, L.; Alsari, M.; She, X. J.; Liang, L.; Zhang, J.; Lilliu, S.; Gao, P.; Snaith, H. J.; Wang, J.; Greenham, N. C.; Friend, R. H.; Di, D. High-Efficiency Perovskite–Polymer Bulk Heterostructure Light-Emitting Diodes. *Nat. Photonics* **2018**, *12*, 783–789.
- (34) Gao, Y.; Shi, E. Z.; Deng, S. B.; Shiring, S. B.; Snaider, J. M.; Liang, C.; Yuan, B.; Song, R. Y.; Janke, S. M.; Liebman-Pelaez, A.; Yoo, P.; Zeller, M.; Boudouris, B. W.; Liao, P. L.; Zhu, C. H.; Blum, V.; Yu, Y.; Savoie, B. M.; Huang, L. B.; Dou, L. T. Molecular Engineering of Organic-Inorganic Hybrid Perovskites Quantum Wells. *Nat. Chem.* **2019**, *11*, 1151–1157.
- (35) Blancon, J. C.; Tsai, H.; Nie, W.; Stoumpos, C. C.; Pedesseau, L.; Katan, C.; Kepenekian, M.; Soe, C. M. M.; Appavoo, K.; Sfeir, M. Y.; Tretiak, S.; Ajayan, P. M.; Kanatzidis, M. G.; Even, J.; Crochet, J. J.; Mohite, A. D. Extremely Efficient Internal Exciton Dissociation through Edge States in Layered 2D Perovskites. *Science* **2017**, *355*, 1288–1291.
- (36) Ren, H.; Yu, S.; Chao, L.; Xia, Y.; Sun, Y.; Zuo, S.; Li, F.; Niu, T.; Yang, Y.; Ju, H.; Li, B.; Du, H.; Gao, X.; Zhang, J.; Wang, J.; Zhang, L.; Chen, Y.; Huang, W. Efficient and Stable Ruddlesden-Popper Perovskite Solar Cell with Tailored Interlayer Molecular Interaction. *Nat. Photonics* **2020**, *14*, 154–163.
- (37) Lin, Y.; Fang, Y.; Zhao, J.; Shao, Y.; Stuard, S. J.; Nahid, M. M.; Ade, H.; Wang, Q.; Shield, J. E.; Zhou, N.; Moran, A. M.; Huang, J. Unveiling the Operation Mechanism of Layered Perovskite Solar Cells. *Nat. Commun.* **2019**, *10*, 1008.
- (38) Liu, J.; Leng, J.; Wu, K.; Zhang, J.; Jin, S. Observation of Internal Photoinduced Electron and Hole Separation in Hybrid Two-Dimensional Perovskite Films. *J. Am. Chem. Soc.* **2017**, *139*, 1432–1435.
- (39) Xu, W.; Hu, Q.; Bai, S.; Bao, C.; Miao, Y.; Yuan, Z.; Borzda, T.; Barker, A. J.; Tyukalova, E.; Hu, Z.; Kawecki, M.; Wang, H.; Yan, Z.; Liu, X.; Shi, X.; Uvdal, K.; Fahlman, M.; Zhang, W.; Duchamp, M.; Liu, J. M.; et al. Rational Molecular Passivation for High-Performance Perovskite Light-Emitting Diodes. *Nat. Photonics* **2019**, *13*, 418–424.
- (40) Cao, D. H.; Stoumpos, C. C.; Farha, O. K.; Hupp, J. T.; Kanatzidis, M. G. 2D Homologous Perovskites as Light-Absorbing Materials for Solar Cell Applications. *J. Am. Chem. Soc.* **2015**, *137*, 7843–7850.
- (41) Cho, H.; Jeong, S. H.; Park, M. H.; Kim, Y. H.; Wolf, C.; Lee, C. L.; Heo, J. H.; Sadhanala, A.; Myoung, N.; Yoo, S.; Im, S. H.; Friend, R. H.; Lee, T. W. Overcoming the Electroluminescence Efficiency Limitations of Perovskite Light-Emitting Diodes. *Science* **2015**, *350*, 1222–1225.
- (42) Shi, J.; Gao, Y.; Gao, X.; Zhang, Y.; Zhang, J.; Jing, X.; Shao, M. Fluorinated Low-Dimensional Ruddlesden-Popper Perovskite Solar Cells with Over 17% Power Conversion Efficiency and Improved Stability. *Adv. Mater.* **2019**, *31*, 1901673.
- (43) Kuang, Y.; Werf, K. H. M. v. d.; Houweling, Z. S.; Schropp, R. E. I. Nanorod Solar Cell with an Ultrathin a-Si:H Absorber Layer. *Appl. Phys. Lett.* **2011**, *98*, 113111.
- (44) Kayes, B. M.; Atwater, H. A.; Lewis, N. S. Comparison of the Device Physics Principles of Planar and Radial *p-n* Junction Nanorod Solar Cells. *J. Appl. Phys.* **2005**, *97*, 114302.
- (45) Zhou, N.; Shen, Y. H.; Li, L.; Tan, S. Q.; Liu, N.; Zheng, G. H. J.; Chen, Q.; Zhou, H. P. Exploration of Crystallization Kinetics in

Quasi Two-Dimensional Perovskite and High Performance Solar Cells. *J. Am. Chem. Soc.* **2018**, *140*, 459–465.

(46) Zhang, Y. L.; Wang, P. J.; Tang, M. C.; Barrit, D.; Ke, W. J.; Liu, J. X.; Luo, T.; Liu, Y. C.; Niu, T. Q.; Smilgies, D. M.; Yang, Z.; Liu, Z. K.; Jin, S. Y.; Kanatzidis, M. G.; Arnassian, A.; Liu, S. Z. F.; Zhao, K. Dynamical Transformation of Two-Dimensional Perovskites with Alternating Cations in the Interlayer Space for High-Performance Photovoltaics. *J. Am. Chem. Soc.* **2019**, *141*, 2684–2694.

(47) Wu, G. B.; Li, X.; Zhou, J. Y.; Zhang, J. Q.; Zhang, X. N.; Leng, X. Y.; Wang, P. J.; Chen, M.; Zhang, D. Y.; Zhao, K.; Liu, S. Z.; Zhou, H. Q.; Zhang, Y. Fine Multi-Phase Alignments in 2D Perovskite Solar Cells with Efficiency Over 17% via Slow Post-Annealing. *Adv. Mater.* **2019**, *31*, 1903889.

(48) Yang, R.; Li, R. Z.; Cao, Y.; Wei, Y. Q.; Miao, Y. F.; Tan, W. L.; Jiao, X. C.; Chen, H.; Zhang, L. D.; Chen, Q.; Zhang, H. T.; Zou, W.; Wang, Y. M.; Yang, M.; Yi, C.; Wang, N. N.; Gao, F.; McNeill, C. R.; Qin, T. S.; Wang, J. P.; et al. Oriented Quasi-2D Perovskites for High Performance Optoelectronic Devices. *Adv. Mater.* **2018**, *30*, 1804771.

(49) Dong, Q.; Fang, Y.; Shao, Y.; Mulligan, P.; Qiu, J.; Cao, L.; Huang, J. Electron-Hole Diffusion Lengths > 175 μm in Solution-Grown $\text{CH}_3\text{NH}_3\text{PbI}_3$ Single Crystals. *Science* **2015**, *347*, 967–970.

(50) Mihailetchi, V. D.; Wildeman, J.; Blom, P. W. M. Space-Charge Limited Photocurrent. *Phys. Rev. Lett.* **2005**, *94*, 126602.

(51) Chen, W.; Wu, Y.; Yue, Y.; Liu, J.; Zhang, W.; Yang, X.; Chen, H.; Bi, E.; Ashraful, I.; Grätzel, M.; Han, L. Efficient and Stable Large-Area Perovskite Solar Cells with Inorganic Charge Extraction Layers. *Science* **2015**, *350*, 944–948.

(52) Proppe, A. H.; Quintero-Bermudez, R.; Tan, H.; Voznyy, O.; Kelley, S. O.; Sargent, E. H. Synthetic Control over Quantum Well Width Distribution and Carrier Migration in Low-Dimensional Perovskite Photovoltaics. *J. Am. Chem. Soc.* **2018**, *140*, 2890–2896.

(53) Han, T. H.; Lee, J. W.; Choi, C.; Tan, S.; Lee, C.; Zhao, Y.; Dai, Z.; De Marco, N.; Lee, S. J.; Bae, S. H.; Yuan, Y.; Lee, H. M.; Huang, Y.; Yang, Y. Perovskite-Polymer Composite Cross-Linker Approach for Highly-Stable and Efficient Perovskite Solar Cells. *Nat. Commun.* **2019**, *10*, 520.

(54) Hu, J.; Oswald, I. W. H.; Stuard, S. J.; Nahid, M. M.; Zhou, N.; Williams, O. F.; Guo, Z.; Yan, L.; Hu, H.; Chen, Z.; Xiao, X.; Lin, Y.; Yang, Z.; Huang, J.; Moran, A. M.; Ade, H.; Neilson, J. R.; You, W. Synthetic Control Over Orientational Degeneracy of Spacer Cations Enhances Solar Cell Efficiency in Two-Dimensional Perovskites. *Nat. Commun.* **2019**, *10*, 1276.

(55) Xing, G.; Mathews, N.; Sun, S.; Lim, S. S.; Lam, Y. M.; Grätzel, M.; Mhaisalkar, S.; Sum, T. C. Long-Range Balanced Electron- and Hole-Transport Lengths in Organic-Inorganic $\text{CH}_3\text{NH}_3\text{PbI}_3$. *Science* **2013**, *342*, 344–347.

(56) Zhang, H.; Liao, Q.; Wu, Y.; Zhang, Z.; Gao, Q.; Liu, P.; Li, M.; Yao, J.; Fu, H. 2D Ruddlesden-Popper Perovskites Microring Laser Array. *Adv. Mater.* **2018**, *30*, 1706186.

(57) Luo, T.; Zhang, Y.; Xu, Z.; Niu, T.; Wen, J.; Lu, J.; Jin, S.; Liu, S. F.; Zhao, K. Compositional Control in 2D Perovskites with Alternating Cations in the Interlayer Space for Photovoltaics with Efficiency Over 18%. *Adv. Mater.* **2019**, *31*, 1903848.

(58) Quan, L. N.; Zhao, Y. B. A.; de Arquer, F. P. G.; Sabatini, R.; Walters, G.; Voznyy, O.; Comin, R.; Li, Y. Y.; Fan, J. Z.; Tan, H. R.; Pan, J.; Yuan, M. J.; Bakr, O. M.; Lu, Z. H.; Kim, D. H.; Sargent, E. H. Tailoring the Energy Landscape in Quasi-2D Halide Perovskites Enables Efficient Green-Light Emission. *Nano Lett.* **2017**, *17*, 3701–3709.

(59) Zheng, K. B.; Chen, Y. N.; Sun, Y.; Chen, J. S.; Chabera, P.; Schaller, R.; Al-Marri, M. J.; Canton, S. E.; Liang, Z. Q.; Pullerits, T. Inter-Phase Charge and Energy Transfer in Ruddlesden-Popper 2D Perovskites: Critical Role of the Spacing Cations. *J. Mater. Chem. A* **2018**, *6*, 6244–6250.